CrystEngComm

PAPER

View Article Online
View Journal | View Issue

Cite this: *CrystEngComm*, 2014, **16**, 10692

Bismuth doping effect on TiO_2 nanofibres for morphological change and photocatalytic performance†

Ming-Chung Wu,* Jyun-Sian Chih and Wei-Kang Huang

Received 1st July 2014,
Accepted 20th September 2014

DOI: 10.1039/c4ce01348d

www.rsc.org/crystengcomm

Doping bismuth ions into photocatalytic materials is one of the most effective methods for preparing highly visible-light-active photocatalysts. In order to develop high-performance photocatalytic materials that are easy to produce, even in industrial quantities, we developed a facile method to prepare bismuth-doped titanium dioxide (Bi-doped TiO_2) by hydrothermal synthesis followed by thermal annealing treatment. Bi-doped TiO_2 can be applied in the field of photodecolorization of organic dye and photocatalytic hydrogen generation. High concentration doping (>5.00 mol%) resulted in the morphological change of Bi-doped TiO_2 from nanofibre to nanorod observed by transmission electron microscopy. The crystal structure evolution and elemental composition were analysed by combining Raman spectroscopy, X-ray crystallography and X-ray photoelectron spectroscopy. For the photodegradation of organic dye methyl orange, all Bi-doped TiO_2 showed less activity than pristine TiO_2 nanofibres under UV irradiation. 5.00 mol% and 10.00 mol% Bi-doped TiO_2 showed higher activities than pristine TiO_2 nanofibres under visible light irradiation. For the photocatalytic hydrogen generation measurement, none of the Bi-doped TiO_2 showed a detectable value under visible light irradiation. However, under UV irradiation, various Bi-doped TiO_2 catalysts exhibited a detectable photocatalytic hydrogen production rate. 0.50 mol% Bi-doped TiO_2 exhibited the highest performance. The result could be due to the relatively lower overpotential for hydrogen production. Our study developed a series of visible-light-active Bi-doped TiO_2 catalysts, and it could replace the traditional TiO_2 catalysts decorated with a high-cost noble metal.

Introduction

Recently, photocatalytic processes have been used to demonstrate several aspects of organic pollutant decomposition and renewable energy production.[1–3] Many photocatalysts have been found to be very active in the treatment of wastewaters for the broad range of organic pollutants that are used by industries and in daily life. Despite many developed photocatalysts, TiO_2 and its derivatives are still in the mainstream of the studies because of their availability, low cost, high and tunable photocatalytic activity, and photostability.[4–6] This enables versatile applications in a variety of fields, among many others, air purification, wastewater treatment, hydrogen generation, and antimicrobial coatings.[7,8] Anatase TiO_2 is often cited as the best choice for energy materials because it is thermally and chemically stable, non-toxic to humans, environmentally friendly, inexpensive, and easy to produce and to use. Anatase TiO_2 still has a great disadvantage. Because of anatase TiO_2's wide bandgap, it only utilizes ultraviolet irradiation of the solar radiation.[9,10] However, ultraviolet light accounts for only 5% of the sunlight's energy. Thus, how to increase the absorption by utilizing the visible spectrum becomes an important issue. Many efforts of doping various metals onto TiO_2 in bulk or on the surface have been carried out to enhance the absorbing ability over the visible spectrum.[11–13] The results showed clear enhancement of activities. However, the photocatalytic activity of metal-doped TiO_2 photocatalysts substantially depends on the character and the concentration of the dopant ions, besides the method of preparation and its thermal and reductive treatment.[14–18] Bismuth-doped TiO_2 (Bi-doped TiO_2) photocatalysts are good photocatalysts in degradation of pollution and dyes. Bi-doped TiO_2 nanofibre photocatalysts that utilize the visible spectrum will have a great potential application in wastewater treatment, because they are separated easily from aqueous solutions after being used.[19,20] Lu *et al.* found that bismuth (Bi) species exist in different forms and the suitable doping of Bi ions can significantly enhance the photocatalytic activity and photocurrent.[21] Furthermore, it was also suggested that the strong

Department of Chemical and Materials Engineering, College of Engineering, Chang Gung University, Taoyuan 33302, Taiwan.
E-mail: mingchungwu@mail.cgu.edu.tw; Fax: +886 3 2118800 ext. 5324; Tel: +886 3 2118800 ext. 3545

† Electronic supplementary information (ESI) available. See DOI: 10.1039/c4ce01348d

chemical signals from Bi species was observed with a higher post-treatment temperature, which has important effects on the photocatalytic activity for hydrogen evolution, decolorization of RhB, and unbiased photocurrent of the TiO_2 photocatalyst.[22–26] Natarajan *et al.* used a sol–gel method to synthesize TiO_2 and Bi–TiO_2 nanoparticles and also used a hydrothermal method to synthesize TiO_2 and Bi–TiO_2 nanotubes. The study revealed that doping TiO_2 with Bi ions did not restrict the formation of a tubular structure during hydrothermal treatment. Also, a lesser amount of rutile phase was formed after Bi doping. The enhancement in surface area confirmed that there was a change in the morphology of TiO_2 from nanoparticles to nanotubes. This morphological change to Bi–TiO_2 nanotubes increased the organic dye degradation rate.[27] A similar hydrothermal method is used in this study, but the main difference is the calcination temperature. In this study, the calcination temperature is higher than that in the reported paper in order to enhance the crystallinity of the photocatalysts and thus improve the photocatalytic activity. Umar *et al.* prepared a series of Bi-doped TiO_2 nanoparticles with various doping concentrations using a facile sol–gel process. They found that the incorporation of Bi ions in the TiO_2 lattice led to efficient separation of charge carriers and the extension of absorption of TiO_2 over the visible spectrum. They also suggested that the 1.0 mol% Bi-doped TiO_2 exhibited the best photocatalytic degradation efficiency for the dye.[28] Ma *et al.* have fabricated a visible-light-active photocatalytic Bi–TiO_2/SBA-15 material. SBA-15 is a mesoporous silica sieve with uniform hexagonal pores and high surface area. The high photocatalytic activity could be attributed to the appropriate amounts of Bi doping. With this doping amount, it was able to not only enhance the photocurrent due to the reduced electron–hole recombination but also extend the absorption spectra from the ultraviolet spectrum to the visible spectrum. They also reported that the optimal Bi/Ti molar ratio is 2.0%.[29]

In this work, we successfully prepared various visible-light-active Bi-doped TiO_2 catalysts with different doping concentrations and searched for the optimal calcination conditions to enhance their photocatalytic properties. We investigated the influence of Bi doping on TiO_2 for the photoinduced decolorization of methyl orange and photocatalytic hydrogen production to understand the modifying role of Bi species in the Bi–TiO_2 catalysts. Moreover, the Bi doping effects on TiO_2 catalysts for photodecolorization of organic dye and photocatalytic hydrogen generation under irradiation with UV and visible light were also measured and discussed in detail. A series of fibre and/or rod-shaped Bi-doped TiO_2 catalysts were developed, and they could replace the TiO_2 catalysts decorated with a high-cost noble metal in the field of the photodegradation of organic dye and photocatalytic hydrogen production.

Experimental details

Bismuth-doped sodium hydrogen titanate nanofibres were prepared by suspending 1.00 g of TiO_2 anatase powder (Acros Organics, 98%) and various amounts of bismuth nitrate (Acros Organics, 99.999%) in 25 mL of 10.0 M NaOH aqueous solution, followed by treatment in a Teflon-lined autoclave at 150 °C for 24 h. The product was washed with deionized water, filtered and dried in air at 70 °C. Then, it was washed with 0.1 M HCl to exchange Na^+ ions for protons. Again, the product was washed with deionized water, filtered and dried in air at 70 °C. Finally, the products doped with various bismuth concentrations were calcined at various temperatures with a heating rate of 5 °C min^{-1} for various calcination times.

For Raman scattering spectra of various Bi-doped TiO_2 samples, these specimens were positioned on a high-resolution piezoelectric stage of the scanning microscope (WiTec, Alpha300S) and excited by a He–Ne laser of 632.8 nm wavelength (25 mW). The laser beam was focused with a 100× objective lens (Nikon plane objective, NA ≈ 0.9), and the diameter of the laser beam focus was about several micrometers. X-ray photoelectron spectrometry (XPS, ULVAC-PHI, Chigasaki, Japan) was used to examine the various Bi-doped TiO_2 samples by using Al K_α radiation with a photoelectron take-off angle of 45° in high vacuum (~10^{-7} torr). Transmission electron microscopy (TEM, JEOL, JEM-ARM200FTH, Japan) was used to observe the microstructures of various Bi-doped TiO_2 samples, and an X-ray diffractometer (XRD, Bruker, D2 phaser with Xflash 430, Germany) was used to measure the crystalline structure. The UV-vis absorption spectra of various Bi-doped TiO_2 samples were measured using an absorption spectrophotometer (JASCO Analytical Instruments, V-630, Japan) in the 300–900 nm wavelength range.

Photocatalytic hydrogen generation tests were carried out by using a 1 : 1 volume ratio mixture of 2.0 L of ethanol and water in which 50.0 mg of a TiO_2-based catalyst was suspended prior to each experiment. The temperature of the mixture was kept near room temperature. For the light source, six lamps were placed in a hexagonal arrangement around the reactor. The light sources include UV-B lamps (Sankyo Denki G15T8E UV-B lamps, the wavelength of maximum emission of the UV-B lamp was ~312 nm, and the power was 8.0 W), UV-A lamps (Sankyo Denki G8T5BLB UV-A lamps, the wavelength of maximum emission of the UV-A lamp was ~352 nm, and the power was 8.0 W) and visible lamps (Goodly F8T5/D visible lamp, and the power was 8.0 W). The distance between each lamp and reactor is about 5.0 cm. To avoid sedimentation of the catalyst powders, nitrogen (99.995%) was bubbled through the reactor with a flow rate of 400 mL min^{-1}, serving also as a purging gas for the evolving gaseous products. The outlet of the reactor was connected to a cold trap, a molecular sieve, and a hydrogen analyzer (Status Scientific Controls Ltd., FGD3).

The Bi-doped TiO_2 samples with various doping concentrations were tested in the degradation of methyl orange, which is a commonly used model reaction in photocatalysis. In a typical experiment, 20.0 mg of the catalyst was sonicated for 2 min in 150 mL of 10 mg L^{-1} methyl orange (Acros Organics, pure) aqueous solution. The suspension was irradiated with

UV-B lamps, UV-A lamps, and visible lamps under vigorous stirring and ambient conditions. Before the actual photodegradation experiments, the suspensions were left to relax for 10 min in order to minimize the error of dye concentration measurements caused by initial surface adsorption. After centrifugation for 15 min at 5000 rpm, the absorption spectra of the retained methyl orange and its derivatives in the supernatant were recorded using an absorption spectrophotometer (JASCO Analytical Instruments, V-630, Japan) in the 300–900 nm wavelength range. The concentrations of methyl orange were calculated from the absorbance at λ = 464 nm extrapolated to a previously plotted calibration curve.

Results and discussion

In this study, we want to find the optimal bismuth doping concentration that results in good photocatalytic activity for Bi-doped TiO_2 catalysts. First, the thermally treated Bi-doped TiO_2 catalysts doped with various bismuth concentrations, 0.25, 0.50, 1.00, 5.00, 10.00, and 20.00 mol%, were measured using a micro Raman spectrometer to observe the phase transformation at various bismuth doping concentrations. Fig. 1 displays the Raman spectra of Bi-doped TiO_2 catalysts doped with various bismuth concentrations calcined at 600 °C for 12 hours. Obviously, Raman spectrum data show that the Bi-doped TiO_2 catalysts with low doping concentration (<5.00 mol%) still exhibit a TiO_2 anatase phase. However, Bi-doped TiO_2 catalysts significantly changed when the doping concentration is higher than 10.00 mol%. There are some small peaks around 150–300 cm^{-1} when the doping concentration is higher than 10.00 mol%, and it may be attributed to the formation of bismuth oxide (Bi_2O_3). The peak at 165 cm^{-1} is attributed to Bi^{3+} and the peak at 203 cm^{-1} is attributed to the Bi–O–Bi bond.[30] The Raman spectra give information about the vibrational modes of Bi-doped TiO_2 catalysts doped with various bismuth concentrations. The anatase TiO_2 shows major Raman bands at 144, 200, 398, 515, 517 and 640 cm^{-1}, but the Raman bands at 515 and 517 cm^{-1} are superimposed. These bands can be attributed to the six Raman-active modes of the anatase phase with the symmetries of E_g, E_g, B_{1g}, A_{1g}, B_{1g}, and E_g, respectively.[31]

The crystalline structures of the thermally treated Bi-doped TiO_2 catalysts with various doping concentrations were also characterized using an X-ray diffractometer. XRD patterns of various Bi-doped TiO_2 catalysts calcined at 600 °C for 12 hours are shown in Fig. 2. The intensity of reflections at 2θ of 25.3° decreased as the Bi doping concentration increased, indicating that Bi ions destroyed the ordering of the lattice. When the Bi doping concentration reached 10.00 mol%, the crystal structure of anatase TiO_2 transformed to another structure. There were some weak reflections at 2θ around 30° when the doping concentration was 10.00 mol%. It could be attributed to the formation of Bi_2O_3 and indicated that when the doping concentration reached 10.00 mol%, a small part of Bi transformed to Bi_2O_3.[32] From Fig. 2, the Bi-doped TiO_2 catalysts with low doping concentration (<5.00 mol%) exhibit a significant anatase phase, and all of the peaks can be perfectly indexed to the body-centred tetragonal lattice structure [JCPDS no. 89-4921] of anatase TiO_2, with lattice constants $a = b = 3.78$ Å and $c = 9.50$ Å. Combined with Raman spectra as shown in Fig. 1, the XRD result is consistent with the result of the Raman measurement.

The actual Bi concentration in Bi-doped TiO_2 is important information to understand the Bi doping effect on TiO_2 nanofibres. The experimental atomic ratios of Bi/Ti and O/Ti in pristine TiO_2 and various Bi-doped TiO_2 were investigated by XPS, and the results are shown in Table 1. The peak position of Ti $2p_{3/2}$ binding energy in pristine TiO_2 and various Bi-doped TiO_2 materials is at 458.5 eV.[33] For Bi doping concentration, the peak positions in Bi_2O_3 included Bi $4f_{7/2}$ (159.3 eV) and Bi $4f_{5/2}$ (164.1 eV).[34] It is interesting to note that Bi/Ti ratios in various Bi-doped TiO_2 materials measured by XPS are smaller than theoretical values. The reason could be due to the fact that synthesized Bi-doped TiO_2 must be washed with deionized water before the calcination process. The peak position of the O 1s binding energy is around 529.0 eV.[33]

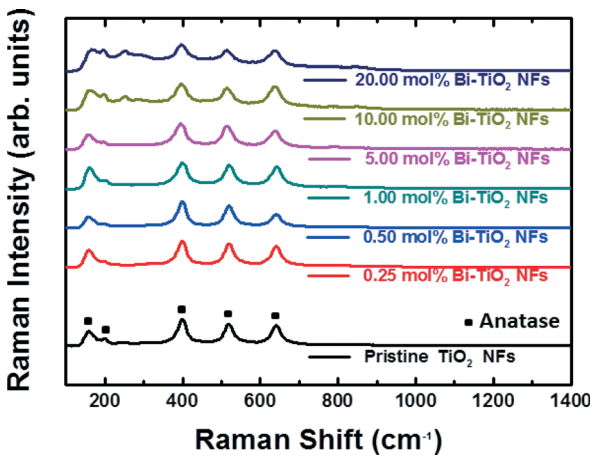

Fig. 1 Raman spectra of the thermally treated Bi-doped TiO_2 catalysts with various doping concentrations.

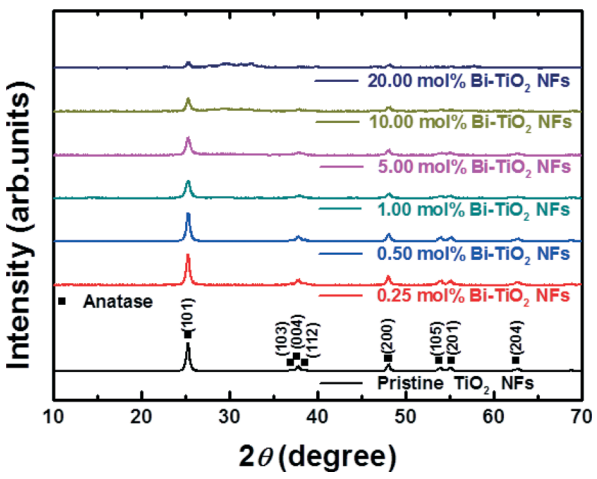

Fig. 2 XRD patterns of the thermally treated Bi-doped TiO_2 catalysts with various doping concentrations.

Table 1 The theoretical and experimental atomic ratios of Bi/Ti and O/Ti in pristine TiO_2 and various Bi-doped TiO_2

Materials	Theoretical value		XPS analysis	
	Bi/Ti (%)	O/Ti (%)	Bi/Ti (%)	O/Ti (%)
Pristine TiO_2	0.00	200.00	0.00	198.02
0.25 mol% Bi–TiO_2	0.25	199.88	0.24	197.01
0.50 mol% Bi–TiO_2	0.50	199.75	0.39	190.08
1.00 mol% Bi–TiO_2	1.00	199.50	0.65	183.15
5.00 mol% Bi–TiO_2	5.26	197.50	3.01	182.16
10.00 mol% Bi–TiO_2	11.11	195.00	8.25	176.22
20.00 mol% Bi–TiO_2	25.00	190.00	17.51	165.35

Moreover, O/Ti ratios in various Bi-doped TiO_2 materials decreased with increasing Bi doping concentration due to the formation of Bi_2O_3. The atomic ratio of O/Ti for TiO_2 is 2.0, but the atomic ratio of O/Bi for Bi_2O_3 is 1.5.

TEM images of the thermally treated Bi-doped TiO_2 catalysts doped with various Bi concentrations are shown in Fig. 3. The as-made pristine TiO_2 material has a length of up to a few micrometres and a diameter of ~100–200 nm (Fig. 3(a)). The morphology of the 0.25 mol% Bi-doped TiO_2 material was similar to that of the pristine TiO_2-NF material, as shown in Fig. 3(b), but some small rod-shaped materials started to appear. The diameter of Bi-doped TiO_2 catalysts decreased to ~100 nm when the doping concentration reached 1.00 mol%, as shown in Fig. 3(c, d). Once the Bi doping concentration reached 5.00 mol% (Fig. 3(e–g)), the Bi-doped TiO_2 catalysts broke into small pieces and became rod-shaped materials (~30–60 nm). Fig. 3(h) shows the high-resolution TEM image of 5.00 mol% Bi-doped TiO_2 material. The high-magnification images of the lattice with the corresponding fast Fourier transform pattern of this specimen are shown in Fig. 3(i, j). Increased *d* spacing for the (101) crystal plane is observed for 5.00 mol% Bi-doped TiO_2. The (101) spacing changed from 3.46 to 3.53 Å.[33] The high-magnification images of the lattice with the corresponding fast Fourier transform pattern of the pristine TiO_2-NFs are shown in Fig. S1 of the ESI.† The results suggested that the Bi doping effect resulted in incorporation of substantial Bi ions into the TiO_2 lattice. The morphological scale of synthesized Bi-doped TiO_2 catalysts decreased as Bi doping concentration increased. The broken microstructure of Bi-doped TiO_2 catalysts was the result of doping Bi ions into TiO_2.

For the photodegradation activity test of various Bi-doped TiO_2 catalysts, we recorded the absorption spectra of methyl orange as a function of UV-A light irradiation time. Then, the

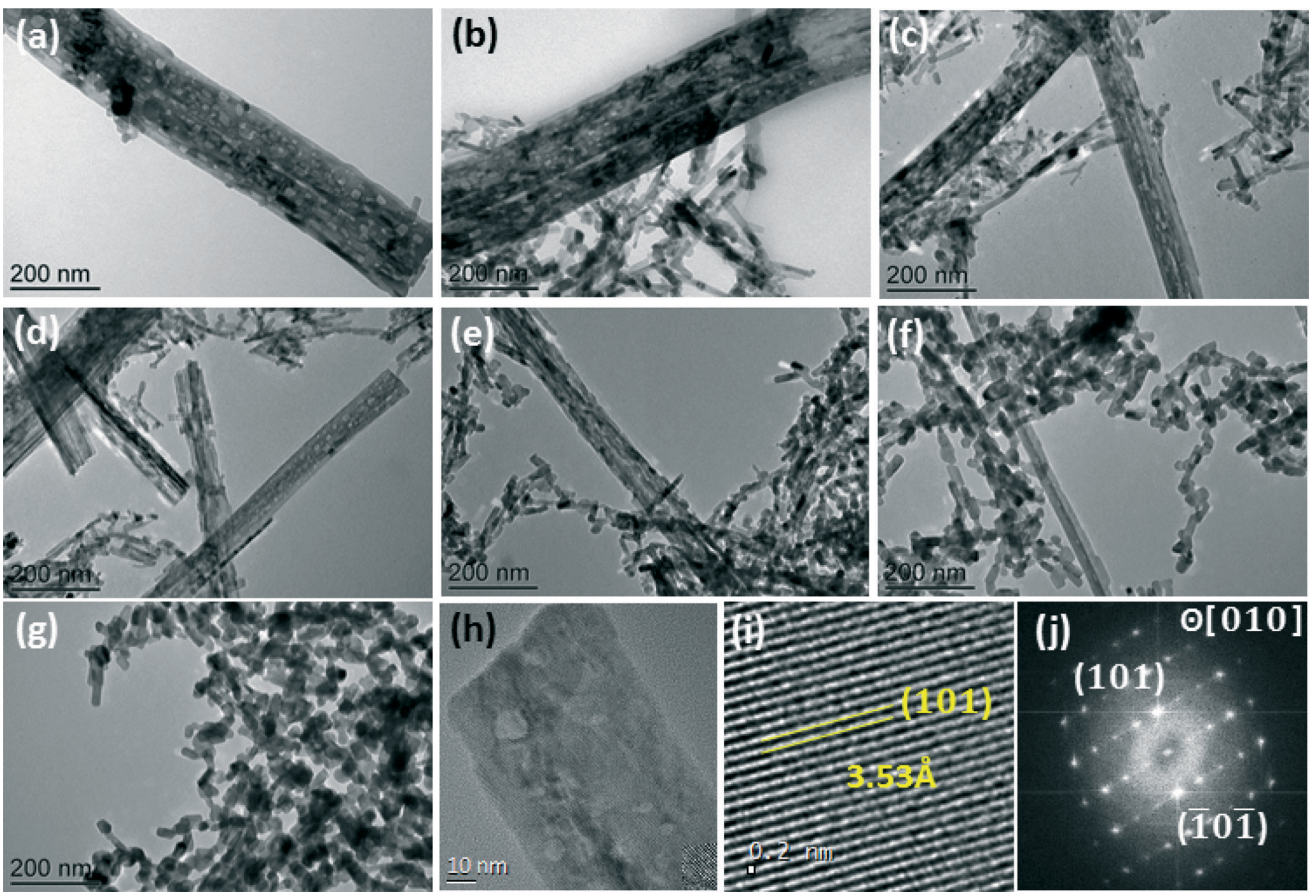

Fig. 3 TEM images of (a) pristine TiO_2 NFs and (b) 0.25 mol%, (c) 0.50 mol%, (d) 1.00 mol%, (e) 5.00 mol%, (f) 10.00 mol%, and (g) 20.00 mol% Bi-doped TiO_2 catalysts. (h) The high-resolution TEM image of 5.00 mol% Bi-doped TiO_2 catalysts and the high-magnification image of the lattice (i) with the corresponding fast Fourier transform pattern of this specimen (j).

absorbance measured at λ = 464 nm was used to calculate the methyl orange concentration using a calibration curve measured previously. The activity of pristine TiO_2 NFs and synthesized Bi-doped TiO_2 catalysts with various doping concentrations for the photodegradation of methyl orange in aqueous solution under UV-A irradiation was measured, and the results are shown in Fig. 4(a). The colour of the suspension changed from the initial orange colour to colourless. TiO_2-catalyzed photodegradation of organic dyes usually follows Langmuir–Hinshelwood kinetics, which can be simplified to an apparent first-order kinetics at lower initial dye concentrations, mathematically described as $\ln(C_0/C) = kt$, where C is the concentration of the dye at time t, C_0 is the initial concentration and k is the apparent reaction rate constant.[35] Plotting the logarithm of the reciprocal of the measured dye concentration as a function of time, we obtained linear slopes for each catalyst we studied, in good agreement with the Langmuir–Hinshelwood model. As shown in Fig. 4(b), the methyl orange decolouration rate showed that the 0.50 mol% Bi-doped TiO_2 catalyst has the highest photodegradation activity among all Bi-doped TiO_2 catalysts. In order to search for the optimal calcination conditions to enhance the photocatalytic activity, we prepared 0.50 mol% Bi-doped TiO_2 catalysts that were calcined for 12 hours in air at various temperatures of 400 °C, 600 °C, 800 °C, and 1000 °C. The photodegradation performance of these Bi-doped TiO_2 catalysts was tested, and the results are shown in Fig. 4(c). The 0.50 mol% Bi-doped TiO_2 catalyst that was calcined at 600 °C showed the highest photocatalytic activity. Finally, we prepared 0.50 mol% Bi-doped TiO_2 catalysts that were calcined at 600 °C for various lengths of time between 3 and 48 hours. The photodegradation performance of these Bi-doped TiO_2 catalysts is shown in Fig. 4(d). Combining the previous three results, the 0.50 mol% Bi-doped TiO_2 catalyst calcined at 600 °C for 12 hours showed the highest activity for photodegradation of methyl orange under UV-A irradiation. Finally, the Bi-doped TiO_2 catalysts with various doping concentrations calcined at 600 °C for 12 hours were used to further study the photodecolourization of organic dye and photocatalytic hydrogen generation under different light sources.

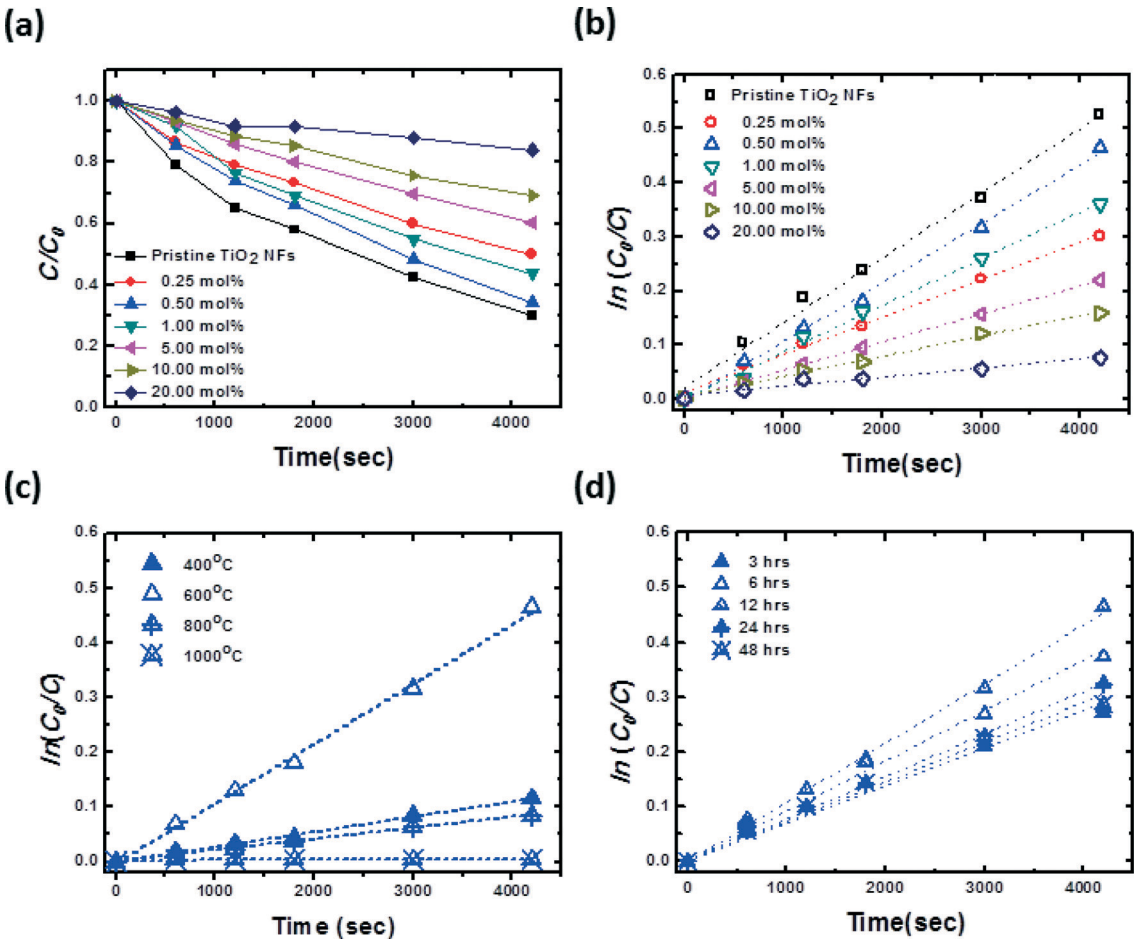

Fig. 4 (a) Activities of pristine TiO_2 NFs and Bi-doped TiO_2 catalysts with various doping concentrations over the photodegradation of methyl orange under UV-A irradiation. (b) Linearized kinetic plots for the degradation of methyl orange using pristine TiO_2 NFs and Bi-doped TiO_2 catalysts with various doping concentrations under UV-A irradiation. (c) Linearized kinetic plots for the degradation of methyl orange using 0.50 mol% Bi-doped TiO_2 catalysts calcined at various temperatures for 12 hours under UV-A irradiation. (d) Linearized kinetic plots for the degradation of methyl orange using 0.50 mol% Bi-doped TiO_2 catalysts calcined for various lengths of time at 600 °C under UV-A irradiation.

In order to understand the correlation between the photodegradation activities and Bi doping concentrations for the catalysts, we measured the photodegradation activities of Degussa P25, pristine TiO_2 NFs and synthesized Bi-doped TiO_2 catalysts under irradiation using various light sources. The significant photocatalytic decolourization was observed under irraditation using different light. The photodegradation reaction rate constants are shown using bar charts in Fig. 5. For the photodegradation activity of these catalysts under UV-B irradiation, as shown in Fig. 5(a), the photodegradation activities decreased with increasing Bi doping concentration. Then, these catalysts were measured under UV-A irradiation. The 0.50 mol% Bi-doped TiO_2 catalyst showed the highest activity among the synthesized Bi-doped TiO_2 catalysts (Fig. 5(b)). Finally, these catalysts were tested under visible-light irradiation. As shown in Fig. 5(c), the 5.00 mol% Bi-doped TiO_2 catalyst showed the highest activity among the synthesized TiO_2 catalysts and Degussa P25. In order to find out the correlation between Bi doping concentration and absorption behaviour, the normalized absorption spectra of pristine TiO_2 NFs and Bi-doped TiO_2 catalysts with various doping concentrations are measured. As shown in Fig. 6, there is a clear extended absorbing ability for Bi-doped TiO_2 catalysts when Bi doping concentration exceeded 0.50 mol%. With increasing Bi doping concentration, much broader absorption was observed. When Bi doping concentration reached 20.00 mol%, there is a very significant change in the absorbance behaviour. From Fig. 6, we can observe that when Bi ions were doped into TiO_2 material, the range of absorption clearly extended to the visible spectrum, which means that the bandgap of the catalyst decreased as Bi doping concentration increased. The bandgaps of pristine TiO_2 NFs and 0.25 mol%, 0.50 mol%, 1.00 mol%, 5.00 mol%, 10.00 mol% and 20.00 mol% Bi-doped TiO_2 are calculated from the UV-vis absorption spectra and their values are 2.92, 2.90,

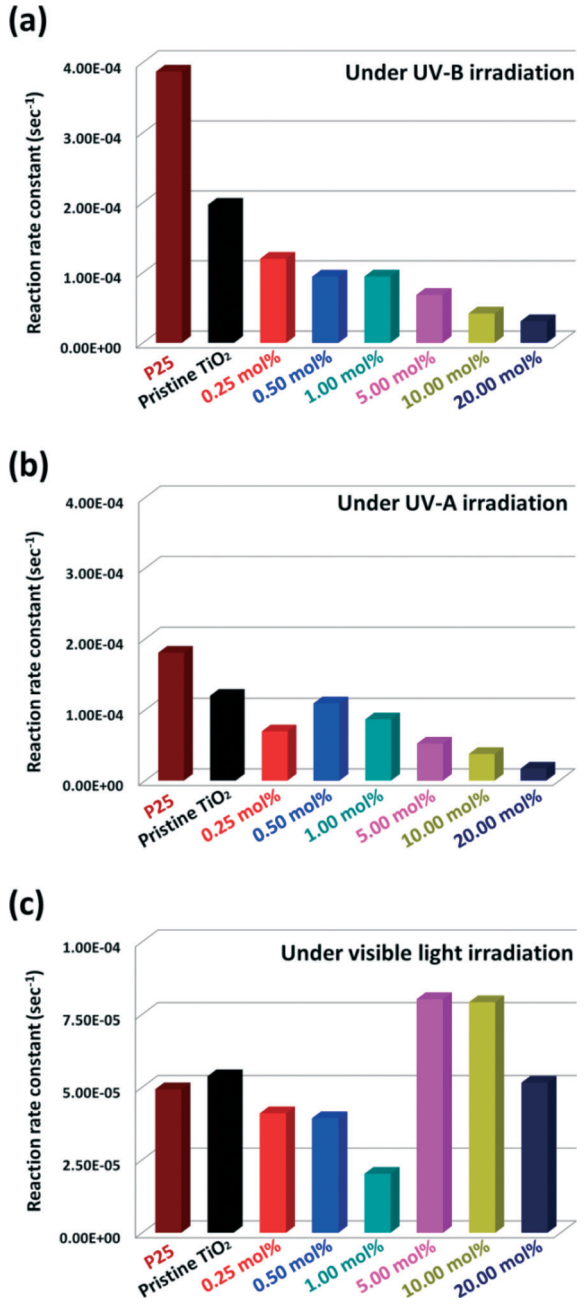

Fig. 5 Bar charts of the photodegradation reaction rate constants of pristine TiO_2 NFs and various Bi-doped TiO_2 catalysts under the following light source irradiation: (a) UV-B, (b) UV-A and (c) visible light.

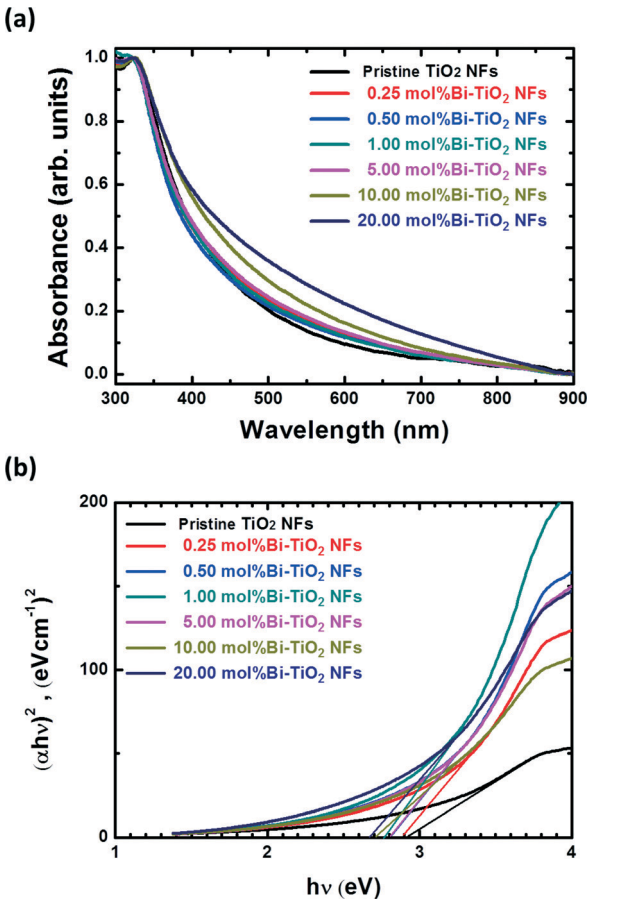

Fig. 6 (a) UV-vis absorption spectra and (b) the bandgaps of pristine TiO_2 NFs and thermally treated Bi-doped TiO_2 catalysts with various Bi doping concentrations.

2.82, 2.78, 2.81, 2.71 and 2.68 eV, respectively. Hence, the 5.00 mol% Bi-doped TiO_2 catalyst and the 10.00 mol% Bi-doped TiO_2 catalyst showed high photodegradation activities under visible light irradiation due to the high photon absorption behaviour in the visible spectrum. Increasing Bi doping concentration resulted in high photon absorption, but it also destroyed the TiO_2 crystalline structure, which hampered the electron/hole transport in the TiO_2 for the 20.00 mol% Bi-doped TiO_2 catalyst.

For the photocatalytic hydrogen generation, Fig. 7 shows the measurement of pristine TiO_2 NFs and various Bi–TiO_2 catalysts under UV-A or UV-B irradiation. As shown in Fig. 7(a) and (b), we observed that pristine TiO_2 NFs showed an undetectable hydrogen generation rate under UV irradiation. The 0.50 mol% Bi-doped TiO_2 catalyst showed the highest rate of photocatalytic hydrogen production. The rates can reach ~800 μmol g^{-1} h^{-1} and ~510 μmol g^{-1} h^{-1} under UV-B and UV-A irradiation, respectively. All Bi-doped TiO_2 catalysts except the 20.00 mol% Bi-doped TiO_2 exhibited photocatalytic hydrogen generation. The photocatalytic hydrogen production rate of Bi-doped TiO_2 catalysts under UV-B irradiation decreased significantly, when the doping concentration exceeded 1.00 mol%. The result could be due to the large amount of Bi doping that altered the crystalline structure, which reduces the electron and/or hole transportation in the materials. However, these catalysts under visible-light irradiation show no detectable value. The results could be due to the low energy of the visible light, which is not enough to excite the TiO_2 catalysts to produce electron/hole pairs. Comparing the two tested reactions under UV-A and UV-B irradiation, the pristine TiO_2 showed good photodegradation of methyl orange dye but showed no detectable value in photocatalytic hydrogen production. The reason could be that the photodegradation reaction is a downhill reaction. As long as the energy of light is greater than the bandgap of the photocatalysts, the reaction would occur. On the other hand, the photocatalytic hydrogen production is an uphill reaction. It means that if the energy levels are coupled with the redox potential of water to generate hydrogen and oxygen, even when the light energy is greater than the bandgap of the photocatalysts, the photocatalytic reaction still would not occur. Bi doping could enhance ethanol oxidation and photoinduced hydrogen evolution, resulting in an increased photocatalytic hydrogen generation rate.

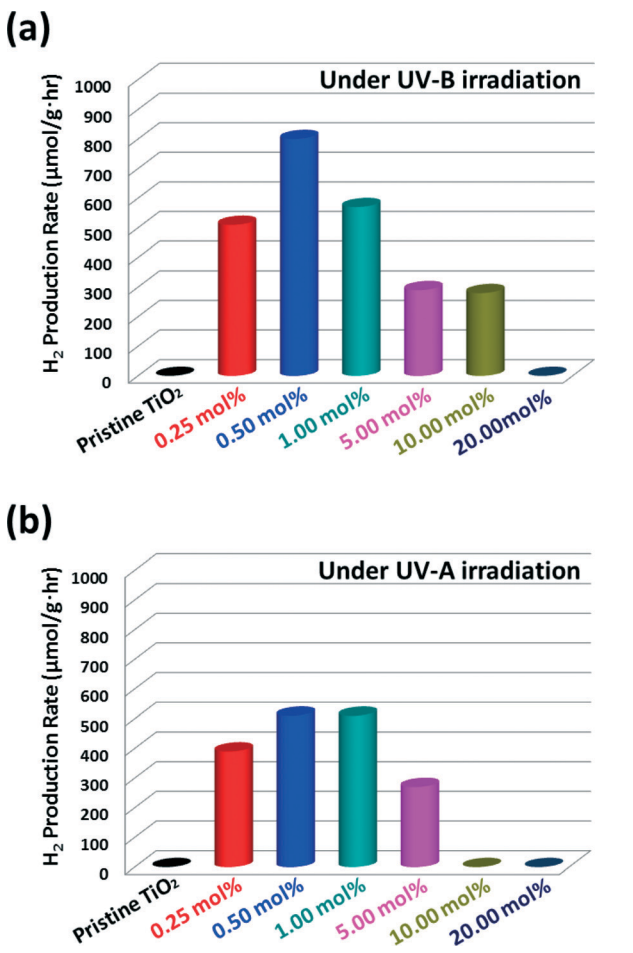

Fig. 7 Bar charts of the hydrogen production rates of pristine TiO_2 NFs and various Bi-doped TiO_2 catalysts under the following light source irradiation: (a) UV-B and (b) UV-A.

Conclusions

In summary, TiO_2 catalysts doped with various Bi concentrations have been synthesized successfully. XRD patterns and Raman spectral analysis confirmed that the high Bi doping concentration can influence the crystalline structure of the catalyst, but Bi doping can extend the absorption of TiO_2 from the UV spectrum to the visible spectrum. Our study focused on the obviously enhancing role of Bi doping of TiO_2 for organic dye decolorization and photocatalytic hydrogen generation. For the photodegradation of methyl orange, all Bi-doped TiO_2 catalysts showed lesser activity than pristine TiO_2 nanofibres under UV irradiation, but the Bi-doped TiO_2 catalysts with high doping concentration (such as 5.00 mol% and 10.00 mol%) showed the highest activity for catalysed photodegradation of methyl orange under visible-light irradiation. For the photocatalytic hydrogen generation measurement, Bi doping could enhance ethanol oxidation and photoinduced hydrogen evolution, resulting in an increased photocatalytic hydrogen generation rate. The 0.50 mol% Bi-doped TiO_2 catalyst showed the highest value of photocatalytic hydrogen production, and the rates can reach ~800 μmol g^{-1} h^{-1} and ~510 μmol g^{-1} h^{-1} under UV-B and UV-A irradiation, respectively. The synthesized Bi-doped TiO_2 catalysts showed the visible spectrum photocatalytic performance, and they could replace the catalysts decorated with a high-cost noble metal.

Acknowledgements

Financial support obtained from the Ministry of Science and Technology of Taiwan (MOST 103-2221-E-182-MY2, MOST 102-2633-E-182-001 and MOST 103-3113-E002-011) and the Chang Gung University Research Project is highly

appreciated. We thank Prof. Wei-Fang Su, Prof. Jing-Jong Shyue and Mr. Chun-Fu Lu of the National Taiwan University and Dr. Ming-Tao Lee's group (BL-13A1) of the National Synchrotron Radiation Research Centre for useful discussions and suggestions.

References

1 A. Fujishima and K. Honda, *Nature*, 1972, **238**, 37.
2 A. J. Nozik, *Nature*, 1975, **257**, 383–386.
3 M. Fujihira, Y. Satoh and T. Osa, *Nature*, 1981, **293**, 206–208.
4 D. Bahnemann, D. Bockelmann and R. Goslich, *Sol. Energy Mater.*, 1991, **24**, 564–583.
5 I. K. Konstantinou and T. A. Albanis, *Appl. Catal., B*, 2004, **49**, 1–14.
6 M. C. Wu, G. Toth, A. Sapi, A. R. Leino, Z. Konya, A. Kukovecz, W. F. Su and K. Kordas, *J. Nanosci. Nanotechnol.*, 2012, **12**, 1421–1424.
7 A. Sarkar, A. Shchukarev, A. Eino, K. Kordas, J.-P. Mikkola, P. Petrov, E. Tuchina, A. Popov, M. Darvin, M. Meinke, J. Lademann and V. Tuchin, *Nanotechnology*, 2012, **23**, 475711.
8 A. Kudo and Y. Miseki, *Chem. Soc. Rev.*, 2009, **38**, 253–278.
9 M. Ni, M. K. H. Leung, D. Y. C. Leung and K. Sumathy, *Renewable Sustainable Energy Rev.*, 2007, **11**, 401–425.
10 F. Fresno, R. Portela, S. Suárez and J. M. Coronado, *J. Mater. Chem. A*, 2014, **2**, 2863.
11 M. A. Fox and M. T. Dulay, *Chem. Rev.*, 1993, **93**, 341–357.
12 M. C. Wu, A. Sápi, A. Avila, M. Szabó, J. Hiltunen, M. Huuhtanen, G. Tóth, Á. Kukovecz, Z. Kónya, R. Keiski, W. F. Su, H. Jantunen and K. Kordás, *Nano Res.*, 2011, **4**, 360.
13 M. Alsawat, T. Altalhi, J. G. Shapterb and D. Losic, *Catal. Sci. Technol.*, 2014, **4**, 2091–2098.
14 D. P. Macwan, P. N. Dave and S. Chaturvedi, *J. Mater. Sci.*, 2011, **46**, 3669–3686.
15 T. Liu and H. Zhang, *RSC Adv.*, 2013, **3**, 16255–16258.
16 T. Huang, S. Mao, J. Yu, Z. Wen, G. Lu and J. Chen, *RSC Adv.*, 2013, **3**, 16657.
17 A. Pandikumar, K. Sivaranjani, C. S. Gopinath and R. Ramaraj, *RSC Adv.*, 2013, **3**, 13390.
18 G. Pótári, D. Madarász, L. Nagy, B. László, A. Sápi, A. Oszkó, A. Kukovecz, A. Erdőhelyi, Z. Kónya and J. Kiss, *Langmuir*, 2013, **29**, 3061–3072.
19 W. Avansi Jr., R. Arenal, V. R. de Mendonça, C. Ribeiro and E. Longo, *CrystEngComm*, 2014, **16**, 5021.
20 J. Xu, W. Wang, M. Shang, E. Gao, Z. Zhang and J. Ren, *J. Hazard. Mater.*, 2011, **196**, 426–430.
21 Y. Wu, G. Lu and S. Li, *J. Phys. Chem. C*, 2009, **113**, 9950–9955.
22 X. H. Xu, M. Wang, Y. Hou, W. F. Yao, D. Wang and H. Wang, *J. Mater. Sci. Lett.*, 2002, **21**, 1655–1656.
23 P. A. K. Reddy, B. Srinivas, P. Kala, V. D. Kumari and M. Subrahmanyam, *Mater. Res. Bull.*, 2011, **46**, 1766–1771.
24 U. G. Akpan and B. H. Hameed, *Appl. Catal., A*, 2010, **375**, 1–11.
25 T. Ji, F. Yang, Y. Lv, J. Zhou and J. Sun, *Mater. Lett.*, 2009, **63**, 2044–2046.
26 D. Dvoranová, V. Brezová, M. Mazúra and M. A. Malati, *Appl. Catal., B*, 2002, **37**, 91–105.
27 T. S. Natarajan, K. Natarajan, H. C. Bajaj and R. J. Tayade, *J. Nanopart. Res.*, 2013, **15**, 1669.
28 S. Sood, S. K. Mehta, A. Umar and S. K. Kansal, *New J. Chem.*, 2014, **38**, 3127.
29 J. Ma, J. Chu, L. Qiang and J. Xue, *RSC Adv.*, 2012, **2**, 3753–3758.
30 M. A. Gondal, T. A. Saleh and Q. Drmosh, *Sci. Adv. Mater.*, 2012, **4**, 507–510.
31 J. Zhang, M. Li, Z. Feng, J. Chen and C. Li, *J. Phys. Chem. B*, 2006, **110**, 927–935.
32 A. P. Periasamy, S. Yang and S. M. Chen, *Talanta*, 2011, **87**, 15–23.
33 M. C. Wu, J. Hiltunen, A. Sápi, A. Avila, W. Larsson, H. C. Liao, M. Huuhtanen, G. Tóth, A. Shchukarev, N. Laufer, A. Kukovecz, Z. Kónya, J. P. Mikkola, R. Keiski, W. F. Su, Y. F. Chen, H. Jantunen, P. M. Ajayan, R. Vajtai and K. Kordás, *ACS Nano*, 2011, **5**, 5025.
34 H. Fan, G. Wang and L. Hu, *Solid State Sci.*, 2009, **11**, 2065.
35 A. Katti, S. R. Venna and M. A. Carreon, *Catal. Commun.*, 2009, **10**, 2036–2040.